

ANALYTIC HI-to-H₂ PHOTODISSOCIATION TRANSITION PROFILES

SHMUEL BIALY*¹ AND AMIEL STERNBERG¹

Accepted for publication in the Astrophysical Journal

ABSTRACT

We present a simple analytic procedure for generating atomic (HI) to molecular (H₂) density profiles for optically thick hydrogen gas clouds illuminated by far-ultraviolet radiation fields. Our procedure is based on the analytic theory for the structure of one-dimensional HI/H₂ photon-dominated regions, presented by Sternberg et al. (2014). Depth-dependent atomic and molecular density fractions may be computed for arbitrary gas density, far-ultraviolet field intensity, and the metallicity dependent H₂ formation rate coefficient, and dust absorption cross section in the Lyman-Werner photodissociation band. We use our procedure to generate a set of HI-to-H₂ transition profiles for a wide range of conditions, from the weak- to strong-field limits, and from super-solar down to low metallicities. We show that if presented as functions of dust optical depth the HI and H₂ density profiles depend primarily on the Sternberg “ αG parameter” (dimensionless) that determines the dust optical depth associated with the total photodissociated HI column. We derive a universal analytic formula for the HI-to-H₂ transition points as a function of just αG . Our formula will be useful for interpreting emission-line observations of HI/H₂ interfaces, for estimating star-formation thresholds, and for sub-grid components in hydrodynamics simulations.

Subject headings: photon-dominated region (PDR) — ISM: clouds — galaxies: star formation — methods: analytical — radiative transfer

1. INTRODUCTION

Stars form in dense molecular hydrogen (H₂) cores that are shielded from external ultraviolet (UV) radiation. The H₂ plays a crucial role in the chemistry that occurs, and its formation leads to the subsequent production of other molecules such as CO, OH and H₂O (e.g., Herbst & Klemperer 1973; Sternberg & Dalgarno 1995; Tielens 2013; van Dishoeck, Herbst & Neufeld 2013; Bialy, Sternberg & Loeb 2015). These species are efficient coolants, and are able to cool the gas to very low temperatures $\sim 10 - 20$ K, reducing the Jeans masses and enabling fragmentation. Star-formation may be triggered by the atomic-to-molecular (HI-to-H₂) phase transition. Alternatively, production of H₂ may be enhanced in the denser and optically thicker gravitationally collapsing components of the interstellar medium (ISM) (Krumholz, Leroy & McKee 2011; Glover & Clark 2012). In any case, the HI-to-H₂ transition is a basic ingredient in any theory of star-formation and galaxy evolution.

Observations of molecular clouds in the Milky-way (e.g., Allen, Heaton & Kaufman 2004; Barriault et al. 2010; Lee et al. 2015; Bialy et al. 2015; Bihr et al. 2015), as well as observations of external galaxies (e.g., Wong & Blitz 2002; Blitz & Rosolowsky 2004; Bigiel et al. 2008; Leroy et al. 2008; Schruba et al. 2011), suggest that the atomic gas converts to molecular form once the HI column density reaches a critical value. Such a threshold is expected since the HI is often a dissociation product of penetrating far-ultraviolet (FUV) radiation in a photon-dominated region (PDR). With increasing column density, the combination of H₂ self-shielding and dust absorption attenuate the radiation field, and a conversion from HI to H₂ occurs.

Theoretically, the HI-to-H₂ conversion in PDRs has

been widely investigated through analytic and numerical studies (e.g., Federman, Glassgold & Kwan 1979; van Dishoeck & Black 1986; Sternberg 1988; Draine & Bertoldi 1996; Kaufman et al. 1999; Browning, Tumlinson & Shull 2003; McKee & Krumholz 2010; Gnedin & Draine 2014; Liszt 2015), as well as in hydrodynamics simulations (e.g., Robertson & Kravtsov 2008; Gnedin, Tassis & Kravtsov 2009; Glover et al. 2010; Bisbas et al. 2012; Davé et al. 2013; Thompson et al. 2014; Lagos et al. 2015).

Sternberg et al. (2014, hereafter S14) presented analytic and detailed radiative transfer computations for the HI-to-H₂ transitions in one dimensional gas slabs irradiated by isotropic or beamed FUV radiation, and with emphasis on the build-up of the photodissociated HI columns in optically thick gas. They considered depth dependent multi-line H₂ photodissociation, and derived analytic formulae for the resulting total HI columns. An important quantity is the dust opacity, $\tau_{1,\text{tot}}$, associated with the total HI column. S14 refer to this as “HI-dust” opacity and derived the analytic expression

$$\tau_{1,\text{tot}} \equiv \sigma_g N_{1,\text{tot}} = \ln \left[\frac{\alpha G}{2} + 1 \right],$$

for a slab exposed to beamed radiation. Here σ_g (cm²) is the metallicity dependent dust absorption cross-section per hydrogen nucleon in the 11.2-13.6 eV Lyman-Werner (LW) photodissociation band, and $N_{1,\text{tot}}$ is the total HI column produced by photodissociation in optically thick clouds, in which all of the radiation is absorbed. The basic dimensionless parameter, αG , that appears in this expression depends on several quantities (see Equation (20) in § 2) and is proportional to the ratio of the FUV intensity to gas density. For realistic ISM conditions αG may range from large ($\gg 1$) to small ($\ll 1$), and the HI dust opacity may or may not be significant.

In this paper, we extend the S14 formalism to develop a simple analytic procedure for the construction of complete depth-dependent atomic and molecular density profiles for

*shmuelbi@mail.tau.ac.il

¹ Raymond and Beverly Sackler School of Physics & Astronomy, Tel Aviv University, Ramat Aviv 69978, Israel

FUV illuminated gas. The “density profiles” are the local volume gas densities of HI and H₂ as functions of cloud depth, as parameterized by the total gas column density, or alternatively by the dust optical depth and/or visual extinction. The analytic procedure we present in this paper provides a simple and quick method to generate such density profiles for a wide range of gas densities and radiation field intensities, and also the H₂ formation efficiencies and dust absorption cross-sections, as specified by the dust-to-gas mass ratio and the overall metallicity. Following the formalism presented in S14, we show that the density profiles depend on the same two parameters, σ_g and αG , that determine the total HI columns. We use our procedure to generate HI-to-H₂ density profiles for a wide range of conditions, including for very low metallicities and dust-to-gas ratios.

Of particular interest are the gas columns and/or dust optical depths at which the conversion from atomic to molecular form occurs. We will show that when expressed in terms of the dust optical depth, the transition points, τ_{tran} , depend almost entirely on just αG , just as for the expression for $\tau_{1,\text{tot}}$. Remarkably, this is irrespective of whether the conversion point is governed by H₂ line self-shielding or HI-dust opacity. We derive a universal fitting formula for the transition optical depth, given by

$$\tau_{\text{tran}} \equiv \sigma_g N_{\text{tran}} = \beta \ln \left[\left(\frac{\alpha G}{2} \right)^{1/\beta} + 1 \right].$$

In this expression N_{tran} is the gas column, atomic *plus* molecular, at which the transition occurs. For dust-to-gas ratios within 0.1 to 10 times the standard ISM value, we find that $\beta = 0.7$ gives the transition point to high accuracy, for any αG .

Our formula will be useful for interpreting observations since the HI/H₂ transition layers are expected sources of ro-vibrational emissions from warm molecules (e.g., Timmermann et al. 1996; Rosenthal, Bertoldi & Drapatz 2000; Rodríguez-Fernández et al. 2001; Allers et al. 2005; Shaw et al. 2009; Sheffer et al. 2011). Our formula will also be useful as a “sub-grid” ingredient in simulations that incorporate atomic to molecular conversion (Gnedin, Tassis & Kravtsov 2009; Mac Low & Glover 2012; Davé et al. 2013; Valdivia & Hennebelle 2014; Thompson et al. 2014; Bahe et al. 2015). This is because with our formula, the transition point may be expressed in terms of external parameters only (i.e. those that enter αG) without requiring a solution for the detailed density profiles or the consideration of molecular self-shielding functions.

The structure of our paper is as follows. In §2 we briefly review the S14 formalism, and elaborate on it to show that αG and σ_g fully determine the HI and H₂ density profiles. In §3 we develop our analytic procedure for the construction of the atomic and molecular density profiles and we present formulae for the necessary auxiliary functions. In §4 we present our set of density profiles computed for a wide range of αG and σ_g , and we discuss their properties. We then derive our fitting formula for the atomic-to-molecular transition points, and also present attenuation factors. In §5 we obtain a threshold for the gas mass surface density required for star-formation. We summarize and conclude in §6.

2. THEORY

In this section we describe the basic analytic theory for the depth dependent variation of the atomic and molecular gas

densities through steady state PDRs. We follow the S14 theoretical framework for semi-infinite gas slabs. S14 considered irradiation by isotropic or beamed fields. Here we assume beamed irradiation.

This theoretical analysis is for H₂ photodissociation by FUV Lyman-Werner photons. H₂ destruction by cosmic-ray and/or X-ray ionization requires a separate treatment (e.g., Maloney, Hollenbach & Tielens 1996; Meijerink & Spaans 2005; Bialy & Sternberg 2015).

2.1. Basic equations

For steady state conditions, and for beamed radiation into one side of an optically thick slab,

$$R n n_1 = \frac{1}{2} D_0 f_{\text{att}} n_2. \quad (1)$$

The left-hand side is the H₂ formation rate per unit volume ($\text{cm}^{-3} \text{s}^{-1}$), where R is the H₂ formation rate coefficient ($\text{cm}^3 \text{s}^{-1}$). The right-hand side is the local (attenuated) photodissociation rate per unit volume, where D_0 is the free-space (unattenuated) photodissociation rate (s^{-1}), and f_{att} is the *depth dependent* attenuation factor accounting for H₂-self shielding and dust absorption. In Equation (1), n_1 and n_2 are the local atomic and molecular volume densities (cm^{-3}) and $n \equiv n_1 + 2n_2$ is the total gas density. For steady state this equality holds at every cloud depth.

The free space H₂ photodissociation rate is $D_0 = \sigma_d \bar{F}_v$, where \bar{F}_v is the mean LW band flux density (photons $\text{cm}^{-2} \text{s}^{-1} \text{Hz}^{-1}$). As computed by S14, $\sigma_d = 2.36 \times 10^{-3} \text{cm}^2 \text{Hz}$ is the total H₂-line photodissociation cross-section, summed over all the lines. For a Draine (1978) far-UV radiation spectrum $\bar{F}_v = 2.46 \times 10^{-8} I_{\text{UV}} \text{photon cm}^{-2} \text{s}^{-1} \text{Hz}^{-1}$, and $D_0 = 5.8 \times 10^{-11} I_{\text{UV}} \text{s}^{-1}$, where I_{UV} is the radiation strength relative to the Draine field, for which $I_{\text{UV}} = 1$. The factor 1/2 in Equation (1) accounts for removal of half of the free-space energy density by the optically thick slab.

Equation (1) is the fundamental relation for PDR theory, and it must be solved, either numerically or analytically, for the depth dependent atomic and molecular volume densities, and the conversion from HI to H₂.

With increasing cloud depth the photodissociation rate is reduced by a combination of H₂-line self-shielding and dust opacity, and the molecular fraction increases. In Equation (1), $f_{\text{att}} \leq 1$ is the attenuation factor,

$$f_{\text{att}}(N_2, N) = f_{\text{shield}}(N_2) e^{-\tau}, \quad (2)$$

and is the product of the dust attenuation term, $e^{-\tau}$, and the H₂-self shielding function $f_{\text{shield}}(N_2)$. Here

$$\tau \equiv \sigma_g N \quad (3)$$

is the dust opacity in the LW band, where $N = N_1 + 2N_2$ is the hydrogen column density, in atoms plus molecules, from the cloud surface to the given cloud depth, and σ_g is the LW band dust absorption cross-section per hydrogen nucleon². In Equation (2) we assume absorption (and pure forward scattering) by the grains, and neglect the (small) effects of back-scattering discussed by Goicoechea & Le Bourlot (2007, see also S14)

²In this paper we are following the S14 notation for which the subscript “d” refers to photo-dissociation, and “g” refers to dust-grains. Thus, σ_d is the photodissociation cross-section, and σ_g is the dust-grain absorption cross section.

The visual extinction is related to τ through

$$\begin{aligned} A_V &= 5.3 \times 10^{-22} N \text{ cm}^2 \text{ mag} \\ &= 0.28 \tau \text{ mag} . \end{aligned} \quad (4)$$

Both σ_g and A_V/N are proportional to the dust-grain surface area, and therefore depend strongly on the dust-to-gas ratio. The dust-to-gas ratio may be further related to the overall gas metallicity.

For standard interstellar dust and assuming a linear relation between the dust-to-gas ratio and gas metallicity

$$\sigma_g = 1.9 \times 10^{-21} \phi_g Z' \text{ cm}^2 , \quad (5)$$

where Z' is the metallicity relative to solar and ϕ_g is a factor of order unity (Draine 2003, S14). For low metallicities the dust-to-gas ratio may scale superlinearly with the metallicity (Rémy-Ruyer et al. 2014) and σ_g will then scale accordingly.

In our discussion below we consider σ_g as a variable, and we define a normalized cross-section

$$\tilde{\sigma}_g \equiv \frac{\sigma_g}{1.9 \times 10^{-21} \text{ cm}^2} , \quad (6)$$

relative to the standard Galactic value.

As discussed in S14, f_{shield} depends on the molecular column, N_2 , only, and its basic definition is

$$f_{\text{shield}}(N_2) \equiv \frac{1}{\sigma_d} \frac{dW_d(N_2)}{dN_2} . \quad (7)$$

In this expression $W_d(N_2)$ is the bandwidth (Hz) of LW radiation absorbed in molecular photodissociations up to N_2 , in a dust-free cloud, and is referred to as the “*dust-free H₂-line dissociation bandwidth*”. Both $W_d(N_2)$ and its derivative $f_{\text{shield}}(N_2)$ are very weakly dependent on the internal molecular excitation state (see S14) and hence may be computed in advance independent of external cloud parameters such as the gas density and field intensity. We discuss analytic forms for $f_{\text{shield}}(N_2)$ and $W_d(N_2)$ in §3.

In Equation (1)

$$\begin{aligned} \alpha &\equiv \frac{D_0}{Rn} = \frac{\sigma_d \bar{F}_V}{Rn} \\ &= 5.8 \times 10^4 I_{\text{UV}} \left(\frac{10^{-17} \text{ cm}^3 \text{ s}^{-1}}{R} \right) \left(\frac{100 \text{ cm}^{-3}}{n} \right) , \end{aligned} \quad (8)$$

is the (dimensionless) ratio of the free-space H₂ photodissociation rate to the H₂ formation rate. The parameter α is proportional to the ratio I_{UV}/n , but it also depends on the H₂ rate coefficient R . The H₂ formation rate coefficient depends on several quantities, including the gas-to-dust ratio and the gas and dust temperatures (e.g., Hollenbach & McKee 1979; Cazaux & Spaans 2004; Le Bourlot et al. 2012). A characteristic value for R is

$$R = 3 \times 10^{-17} \tilde{\sigma}_g \text{ cm}^3 \text{ s}^{-1} , \quad (9)$$

with the further assumption that $R \propto \sigma_g$ since both quantities depend on the dust-grain surface areas. This gives

$$\alpha = 1.9 \times 10^4 I_{\text{UV}} \left(\frac{100 \text{ cm}^{-3}}{n} \right) \frac{1}{\tilde{\sigma}_g} . \quad (10)$$

Therefore, as long as H₂ formation is dominated by dust catalysis, α is inversely proportional to the dust absorption cross-section. For very low metallicities, H₂ formation is dominated by gas phase reactions (e.g., Cazaux & Spaans 2004; Bialy & Sternberg 2015), independent of σ_g .

In terms of α , Equation (1) may be rewritten as

$$\frac{n_1}{n_2} = \frac{1}{2} \alpha f_{\text{att}} . \quad (11)$$

At the cloud boundary $f_{\text{att}} \rightarrow 1$ and the HI to H₂ density ratio $n_1/n_2 \rightarrow 0.5\alpha$. Since $n = n_1 + 2n_2$ the HI and H₂ fractions at the cloud boundary are $2n_2/n = 1/(1 + 0.25\alpha)$ and $n_1/n = 0.25\alpha/(1 + 0.25\alpha)$. For most astrophysical conditions $\alpha \gg 1$ and the gas is predominantly atomic at the unshielded boundaries, with $n_1/n \simeq 1$ and $2n_2/n \simeq 4/\alpha$.

The essential problem is to solve Equation (11) for n_1 and n_2 as functions of cloud depth, as parameterized by the gas column $N = N_1 + 2N_2$ (or visual extinction via Equation (4)). The solution is non-trivial because the attenuation factor depends on N_2 and N in combination, not just on N alone. Thus, to obtain a solution for $n_1(N)$ and $n_2(N)$, one has to first solve for N_2 as a function of N .

2.2. No dust absorption

A simplifying case is the limit where dust absorption is negligible, i.e. $\tau \ll 1$, for which $f_{\text{att}} \rightarrow f_{\text{shield}}$ and self-shielding dominates. Assuming Rn constant, and with Equation (7) for f_{shield} , and with $n_1/n_2 = dN_1/dN_2$ for slab geometry, integration gives

$$N_1(N_2) = \frac{1}{2} \alpha \frac{W_d(N_2)}{\sigma_d} = \frac{1}{2} \frac{\bar{F}_V W_d(N_2)}{Rn} , \quad (12)$$

for the accumulated HI column as a function of N_2 . For any α , and given the precomputed $W_d(N_2)$, and with $N \equiv N_1 + 2N_2$, Equation (12) gives $N_1(N)$ and $N_2(N)$.

Equation (11) with $n \equiv n_1 + 2n_2$ then gives $n_1(N)$ and $n_2(N)$. Thus, when dust absorption is negligible, the HI and H₂ density profiles are fully determined by the dimensionless parameter α . This solution is valid only up to gas columns $N \lesssim 5 \times 10^{20} / \tilde{\sigma}_g \text{ cm}^{-2}$ (for which $\tau \lesssim 1$). For larger columns, dust absorption becomes significant.

2.3. Inclusion of dust absorption

With the inclusion of dust absorption, f_{att} becomes a function of both N_2 and N , and σ_g enters as a parameter. However, since $e^{-\tau} \equiv e^{-\sigma_g N} = e^{-\sigma_g N_1} \times e^{-2\sigma_g N_2}$, Equation (11) is separable and may be written as

$$\begin{aligned} e^{\sigma_g N_1} dN_1 &= \frac{\alpha}{2} f_{\text{shield}}(N_2) e^{-2\sigma_g N_2} dN_2 \\ &= \frac{\alpha}{2} \frac{1}{\sigma_d} \frac{dW_g}{dN_2} dN_2 , \end{aligned} \quad (13)$$

where again $n_1/n_2 = dN_1/dN_2$, as appropriate for slab geometry. With this separation, and again assuming that Rn is constant through the cloud, N_1 can still be expressed as a function of N_2 , as follows.

The derivative on the right-hand side of Equation (13) is of the function

$$\begin{aligned} W_g(N_2; \sigma_g) &\equiv \int_0^{N_2} \frac{dW_d(N'_2)}{dN'_2} e^{-2\sigma_g N'_2} dN'_2 \\ &= \sigma_d \int_0^{N_2} f_{\text{shield}}(N'_2) e^{-2\sigma_g N'_2} dN'_2 . \end{aligned} \quad (14)$$

Importantly, the exponential term in the integrand definition of $W_g(N_2; \sigma_g)$ accounts for the dust opacity associated with the H₂ column only (“H₂-dust”). Thus, as discussed in S14,

$W_g(N_2; \sigma_g)$ is the “ H_2 -dust limited dissociation bandwidth”. $W_g(N_2; \sigma_g)$ may be viewed as a curve-of-growth for the accumulating absorption of dissociating photons in a cloud that is fully molecular but also dusty. The function $W_g(N_2; \sigma_g)$ may be computed in advance for any assumed σ_g , and is independent of the gas density or the radiation field strength. S14 presented detailed numerical radiative transfer computations for $W_g(N_2; \sigma_g)$.

For small H_2 columns, H_2 -dust absorption is negligible compared to H_2 -line absorption so that $W_g(N_2) \rightarrow W_d(N_2)$, and the solutions approach the dust-free solutions given by Equation (12). For larger H_2 columns $W_g(N_2) < W_d(N_2)$ when some of the LW photons are absorbed by H_2 -dust rather than in H_2 photodissociations. For sufficiently large H_2 columns the dissociation bandwidth reaches a total (asymptotic) value. Following S14 we refer to this asymptotic bandwidth as $W_{g,\text{tot}}(\sigma_g)$. The asymptotic bandwidth is maximal for complete H_2 line overlap, and is reduced by H_2 -dust opacity for sufficiently large $\tilde{\sigma}_g$. The product $(1/2)\bar{F}_v W_{g,\text{tot}}$ is then the *effective* dissociation photon flux absorbed by H_2 in photodissociations, excluding photons absorbed by H_2 -dust, in fully molecular gas.

It is convenient to also define the normalized (dimensionless) curve-of-growth

$$\tilde{w}(N_2; \sigma_g) \equiv \frac{W_g(N_2; \sigma_g)}{W_{g,\text{tot}}(\sigma_g)}, \quad (15)$$

which has the property that for any σ_g , $\tilde{w} \rightarrow 1$ as $N_2 \rightarrow \infty$. In §3 we plot the functions W_g , \tilde{w} , and $W_{g,\text{tot}}$ (Figs. 2 and 3) and also derive analytic forms for these quantities based on the numerical radiative transfer results presented by S14.

Equation (13) may be integrated with N_2 the independent variable. This gives

$$N_1(N_2) = \frac{1}{\sigma_g} \ln \left[\frac{\alpha G}{2} \tilde{w}(N_2; \sigma_g) + 1 \right]. \quad (16)$$

In this expression

$$\begin{aligned} G &\equiv \frac{\sigma_g}{\sigma_d} W_{g,\text{tot}} \\ &= 3.0 \times 10^{-5} \tilde{\sigma}_g \left(\frac{9.9}{1 + 8.9\tilde{\sigma}_g} \right)^{0.37}, \end{aligned} \quad (17)$$

where we have used the analytic form we develop for $W_{g,\text{tot}}(\tilde{\sigma}_g)$ in §3.3 below (Equation (29)). As discussed by S14, the parameter G is generally $\ll 1$, and may be viewed as the average H_2 -self shielding attenuation factor, averaged over an H_2 -dust optical depth ~ 1 . The product $D_0 G$ is then the characteristic shielded dissociation rate.

With the inclusion of dust absorption, Equation (16) replaces Equation (12) for $N_1(N_2)$. Together with $N = N_1 + 2N_2$ this gives N_1 and N_2 as functions of the gas column N . This then gives the attenuation factor, f_{att} , as a function of N alone, determining the density profiles n_1 and n_2 versus the total gas column.

2.4. Total HI column and the αG parameter

For $N_2 \rightarrow \infty$, $\tilde{w} \rightarrow 1$, and we recover the basic S14 expression for the total HI column density

$$N_{1,\text{tot}} = \frac{1}{\sigma_g} \ln \left[\frac{\alpha G}{2} + 1 \right]. \quad (18)$$

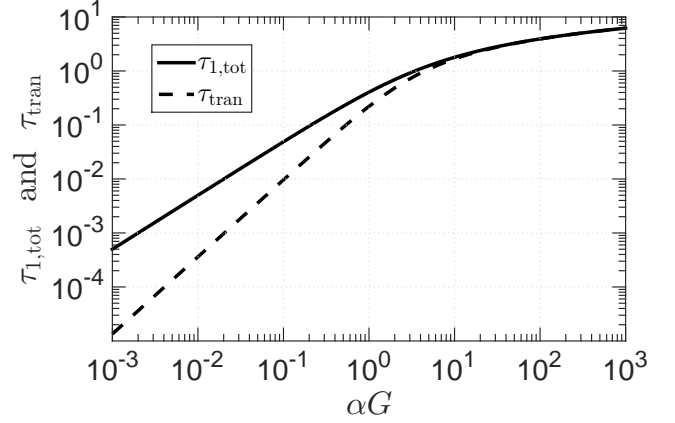


FIG. 1.— The total HI-dust opacity $\tau_{1,\text{tot}} \equiv \sigma_g N_{1,\text{tot}}$ (solid) and the dust opacity at the HI-to- H_2 transition point $\tau_{\text{tran}} \equiv \sigma_g N_{\text{tran}}$ (dashed), as functions of the basic dimensionless parameter αG (see text).

This is for one side of an optically thick slab irradiated by a beamed field. The HI dust opacity associated with the total HI column is then simply

$$\tau_{1,\text{tot}} \equiv \sigma_g N_{1,\text{tot}} = \ln \left[\frac{\alpha G}{2} + 1 \right]. \quad (19)$$

In Equation (18) and (19) the dimensionless parameter is

$$\alpha G \equiv \frac{D_0}{Rn} \frac{\sigma_g}{\sigma_d} W_{g,\text{tot}} = \frac{\sigma_g \bar{F}_v W_{g,\text{tot}}}{Rn}, \quad (20)$$

and it accounts for both H_2 self-shielding and dust absorption. This was a key result in S14 (see also Sternberg 1988). The basic dimensionless parameter for $\tau_{1,\text{tot}}$ is always αG , not α alone. As shown by Equation (20), αG may be expressed as the ratio of the shielded dissociation rate to the H_2 formation rate. Alternatively, it is the ratio of the HI-dust absorption rate of the effective dissociation flux to the H_2 formation rate.

Using Equations (8) and (17) for α and G we may write αG in the normalized form

$$\begin{aligned} \alpha G &= 1.76 I_{\text{UV}} \tilde{\sigma}_g \left(\frac{10^{-17} \text{ cm}^3 \text{ s}^{-1}}{R} \right) \left(\frac{100 \text{ cm}^{-3}}{n} \right) \\ &\times \left(\frac{9.9}{1 + 8.9\tilde{\sigma}_g} \right)^{0.37}. \end{aligned} \quad (21)$$

For H_2 formation on dust grains (Equation (9)),

$$\alpha G = 0.59 I_{\text{UV}} \left(\frac{100 \text{ cm}^{-3}}{n} \right) \left(\frac{9.9}{1 + 8.9\tilde{\sigma}_g} \right)^{0.37}. \quad (22)$$

Like α , the product αG is also proportional to the ratio I_{UV}/n , but the prefactor is of order unity. Both large and small αG are relevant for the realistic range of interstellar conditions. The remaining factor $1/(1 + 8.9\tilde{\sigma}_g)^{0.37}$ accounts for the reduction in the total dissociation bandwidth by H_2 -dust absorption, which becomes important for $\tilde{\sigma}_g \gtrsim 0.1$. Because αG itself depends on $\tilde{\sigma}_g$, the ratio I_{UV}/n must be adjusted if αG is held constant for varying $\tilde{\sigma}_g$. For example, for $\alpha G = 1$, $I_{\text{UV}}/n = 9 \times 10^{-3}$, 2×10^{-2} , and $4 \times 10^{-2} \text{ cm}^3$, for $\tilde{\sigma}_g = 0.1$, 1, and 10.

In Fig. 1 we plot $\tau_{1,\text{tot}}$ as a function of αG (solid curve). For $\alpha G \ll 1$, $\tau_{1,\text{tot}}$ increases linearly with αG . This is the “weak-field” limit. For $\alpha G \gtrsim 1$, $\tau_{1,\text{tot}} \gtrsim 1$, HI-dust dominates the absorption of the LW-band radiation, and the HI column is “self-limited”. This is the “strong-field” limit.

For $\alpha G \ll 1$, $\tau_{1,\text{tot}} \ll 1$ and HI-dust absorption is negligible. In this limit $N_1(N_2) \rightarrow 0.5\alpha G \tilde{w}/\sigma_g = 0.5\alpha W_g/\sigma_d$ (notice that σ_g drops out). If H₂-dust is also negligible $W_g \rightarrow W_d$ and we recover Equation (12) for the dust-free conditions.

In Fig. 1 we also plot (dashed curve) the analytic expression we derive in §4.3 for the dust optical depth τ_{tran} , at which the HI-to-H₂ transition occurs (see Equation (39)). We first present our procedure for generating the atomic and molecular density profiles. These will determine the transition points as functions of αG and $\tilde{\sigma}_g$.

2.5. Time-scales

The above analysis, beginning with the formation-destruction Equation (1) is for steady state conditions. The time-scale to reach steady-state is given by

$$t_{\text{eq}} = \frac{1}{D + 2Rn}, \quad (23)$$

where D is the local (attenuated) photodissociation rate and Rn is the formation rate. When $D/(2Rn) \gg 1$, t_{eq} is the dissociation time $\simeq 1/D$, and the gas becomes atomic on a short time-scale. For example, in free-space $D = D_0$ and $t_{\text{eq}} \approx 5.5 \times 10^2 / I_{\text{UV}}$ yr. When $D/(2Rn) \ll 1$, t_{eq} is the molecular formation time $\simeq 1/(2Rn) \approx 5 \times 10^8 / n$ yr. Because the molecular formation time is long, non-equilibrium effects (e.g., Liszt 2007) may become important beyond the HI-to-H₂ transition points.

3. ANALYTIC PROCEDURE FOR GENERATING PROFILES

Differentiating Equation (16) gives a formal expression for the atomic-to-molecular density ratio as a function of just the molecular column,

$$\frac{n_1}{n_2}(N_2) = \frac{1}{\sigma_g} \times \frac{\alpha G \tilde{w}'(N_2; \sigma_g)}{\alpha G \tilde{w}(N_2; \sigma_g) + 2}, \quad (24)$$

where $\tilde{w}' \equiv d\tilde{w}/dN_2$. Together with Equation (16) this can be converted to n_1/n_2 as a function of the total gas column N , since $N = N_1(N_2) + 2N_2$. Because the functions on the right-hand-sides of Equations (16) and (24) depend on just σ_g and αG , so do n_1/n_2 , n_1/n and n_2/n , all as functions of N .

Equation (24) can be reexpressed in the computationally convenient form

$$\begin{aligned} \frac{n_1}{n_2}(N_2) &= \frac{\alpha f_{\text{shield}}(N_2) e^{-2\sigma_g N_2}}{\alpha G \tilde{w}(N_2; \sigma_g) + 2} \\ &= \left(\frac{\sigma_d}{\sigma_g} \right) \frac{\alpha G f_{\text{shield}}(N_2) e^{-2\sigma_g N_2}}{\alpha G W_g(N_2; \sigma_g) + 2W_{g,\text{tot}}(\sigma_g)}. \end{aligned} \quad (25)$$

The depth-dependent atomic and molecular densities may then be constructed in a simple procedure:

1. Select values for σ_g and αG (Equations (6) and (22)).
2. Evaluate n_1/n_2 as a function of N_2 using Equation (25), with the analytic forms for f_{shield} , W_g , and $W_{g,\text{tot}}$ (Equations (26), (27), and (29) below).
3. Compute $N_2(N)$ using Equation (16) for $N_1(N_2)$ together with the relation $N = N_1 + 2N_2$.
4. Convert n_1/n_2 versus N_2 to n_1/n_2 as a function of N .
5. Obtain n_1/n and $2n_2/n$ as functions of N , assuming constant gas density $n \equiv n_1 + 2n_2$.

In the remainder of this section we provide the analytic expressions for f_{shield} , W_g , and $W_{g,\text{tot}}$, required to evaluate Equation (25).

3.1. Self-shielding function $f_{\text{shield}}(N_2)$

The self-shielding function $f_{\text{shield}}(N_2)$ as defined by Equation (7) was computed via multi-line radiative transfer in S14. The results (see Fig. 2 of S14) are in excellent agreement with the Draine & Bertoldi (1996) fitting function

$$\begin{aligned} f_{\text{shield}} &= \frac{0.965}{(1+x/b_5)^2} + \frac{0.035}{(1+x)^{0.5}} \\ &\times \exp[-8.5 \times 10^{-4}(1+x)^{0.5}]. \end{aligned} \quad (26)$$

Here, $x \equiv N_2/(5 \times 10^{14} \text{ cm}^{-2})$ and $b_5 \equiv b/(10^5 \text{ cm s}^{-1})$ is the normalized Doppler parameter. In our computations we assume $b_5 = 2$ as a compromise between purely thermal and turbulent broadened linewidths. As we discuss further below (§4.2) the positions of the transition points depend weakly on b .

In Fig. 2 (upper panel) we plot f_{shield} as a function of N_2 for $b_5 = 1, 2$, and 4. The onset of self-shielding occurs at small H₂ columns, $\sim 10^{14} \text{ cm}^{-2}$, the exact value depending on b . At $N_2 \gtrsim 10^{17} \text{ cm}^{-2}$ the absorption occurs out of the radiative damping wings and the self-shielding is independent of the Doppler parameter. Finally, at very large columns, $N_2 \gtrsim 10^{22} \text{ cm}^{-2}$, the absorption lines overlap and f_{shield} drops sharply.

As we discuss in §4.3 below in our analysis of the transition points, a simple power-law approximation $f_{\text{shield}} \propto N_2^{-\beta}$, is useful. For the range $10^{14} < N < 10^{21.5} \text{ cm}^{-2}$, a power law index $\beta = 0.7$ provides a good approximation. This is shown as the red dotted line in Fig. 2 (upper panel).

3.2. H₂-dust limited dissociation bandwidth $W_g(N_2; \sigma_g)$

S14 presented radiative transfer computations for the H₂-dust limited dissociation bandwidth, $W_g(N_2; \sigma_g)$, for four discrete values of σ_g , ranging from $\tilde{\sigma}_g = 0.01$ to 10. Recall, $\tilde{\sigma}_g$ is the normalized dust cross section, normalized to $1.9 \times 10^{-21} \text{ cm}^2$. Those computations were carried out using the Meudon PDR code³. The numerical S14 results for $W_g(N_2; \sigma_g)$ are the circles in Fig. 2 (middle panel). For our purposes we require analytic expressions that vary smoothly with N_2 for any σ_g within this range. We find that an excellent fit to the S14 calculations is

$$W_g(N_2; \tilde{\sigma}_g) = a_1 \ln \left[\frac{a_2 + y}{1 + y/a_3} \right] \left(\frac{1 + y/a_3}{1 + y/a_4} \right)^{0.4}, \quad (27)$$

where

$$\begin{aligned} y &\equiv \frac{N_2}{10^{14} \text{ cm}^{-2}} \\ a_1 &= 3.6 \times 10^{11} \text{ Hz} \\ a_2 &= 0.62 \\ a_3 &= 2.6 \times 10^3 \\ a_4 &= 1.4 \times 10^7 \times (1 + 8.9\tilde{\sigma}_g)^{-0.93}. \end{aligned}$$

The analytic fits are displayed as the solid curves in Fig. 2 (middle panel). Our analytic formula for $W_g(N_2; \sigma_g)$ is accu-

³Publicly available at <http://pdr.obspm.fr>

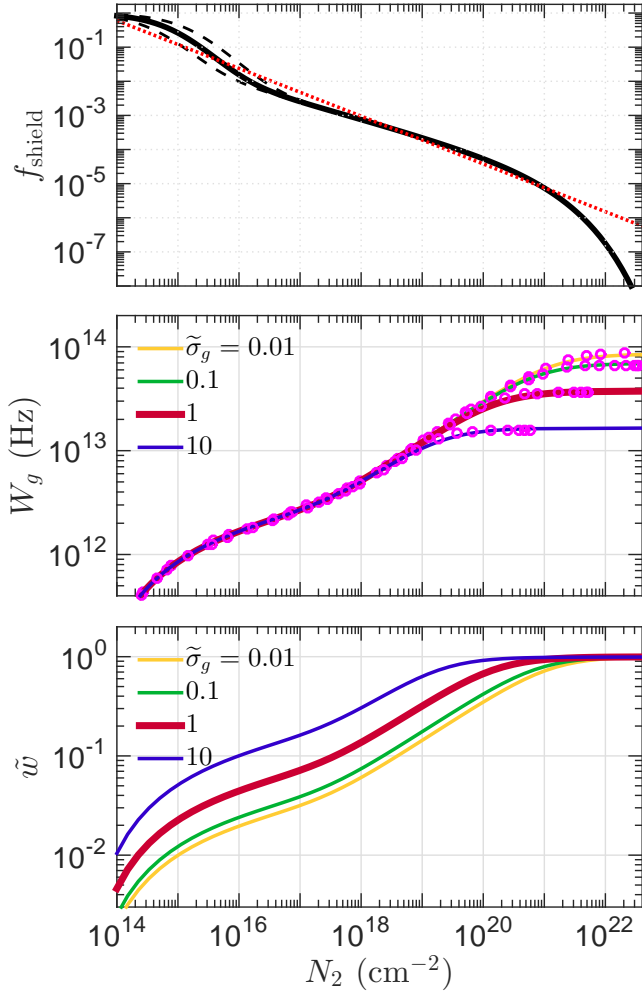


FIG. 2.— Top: The H₂-self shielding function f_{shield} as a function of the H₂ column N_2 , for three values of Doppler parameters $b_5 = 2$ (solid) $b_5 = 1$ (upper dashed), and $b_5 = 4$ (lower dashed). The red dotted line is the power law approximation $f_{\text{shield}} \propto N_2^{-0.7}$. Middle: The H₂-dust limited dissociation bandwidth W_g , for various values of the normalized dust cross section $\tilde{\sigma}_g$. The circles are the radiative transfer calculations and the solid colored curves are our fit, given by Equation (27). For small N_2 , W_g is independent of $\tilde{\sigma}_g$ and is similar to a single-line absorption. For large N_2 , all the UV photons are absorbed and W_g reaches an asymptotic value $W_{g,\text{tot}}$. Bottom: the normalized curve of growth $\tilde{w} \equiv W_g/W_{g,\text{tot}}$.

rate to within 6 % of the numerical results for $N_2 > 10^{14} \text{ cm}^{-2}$ and for any $\tilde{\sigma}_g \leq 10$.

The form of our fitting function Equation (27), is physically motivated by “the curve of growth” behavior of the dissociation bandwidth, which up to the H₂-dust cutoff closely resembles that for a simple absorption line. For small H₂ columns ($y \lesssim a_2$), the photons are absorbed in optically thin Doppler-cores and $W_g \propto N_2$, i.e. the linear regime. For intermediate columns ($a_2 \lesssim y \lesssim a_3$), $W_g \propto \ln[N_2]$, corresponding to the flat part of the curve-of-growth. At large columns ($a_3 \lesssim y \lesssim a_4$) absorption is dominated by the damping wings, and W_g scales as a power law of N_2 . Finally, for very large columns ($y \gtrsim a_4$), the LW photons are either fully absorbed in overlapping H₂ lines or by H₂-dust. Either way, W_g flattens. H₂-dust dominates the cutoff for $\tilde{\sigma}_g \gtrsim 0.1$ and a_4 is then sensitive to $\tilde{\sigma}_g$. For $\tilde{\sigma}_g \ll 0.1$, H₂-dust is negligible and the entire LW band is absorbed in overlapping H₂ lines. In this limit $W_g(N_2; \sigma_g) \rightarrow W_d(N_2)$ and is maximal, reaching

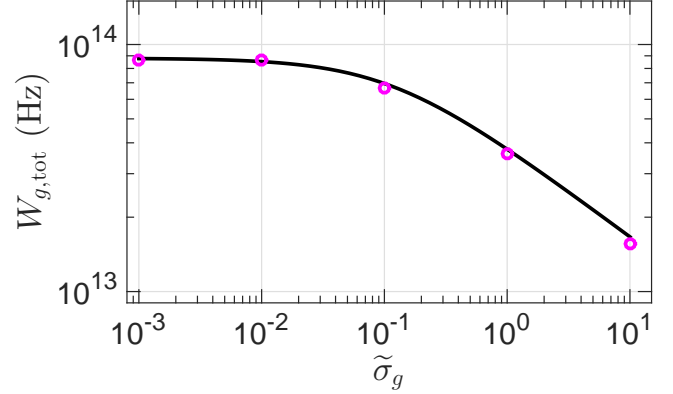


FIG. 3.— The total H₂-dissociation bandwidth $W_{g,\text{tot}}$ as function of the normalized dust cross section $\tilde{\sigma}_g$. The magenta circles are the explicit radiative transfer calculations of S14, and the solid curve is our analytic formula, Equation (29).

$8.8 \times 10^{13} \text{ Hz}$, independent of $\tilde{\sigma}_g$.

3.3. Total dissociation bandwidth $W_{g,\text{tot}}(\sigma_g)$

As N_2 becomes large $W_g(N_2; \sigma_g)$ approaches the total H₂-dust limited dissociation bandwidth $W_{g,\text{tot}}(\sigma_g)$. The circles in Fig. 3 are the radiative transfer numerical results as computed by S14 for $W_{g,\text{tot}}(\sigma_g)$. S14 also presented the fitting function

$$W_{g,\text{tot}}^{\text{S14}}(\tilde{\sigma}_g) = \frac{9.9 \times 10^{13} \text{ Hz}}{1 + (2.6\tilde{\sigma}_g)^{1/2}}. \quad (28)$$

Here we adopt an alternative and more accurate expression

$$W_{g,\text{tot}}(\tilde{\sigma}_g) = \frac{8.8 \times 10^{13} \text{ Hz}}{(1 + 8.9\tilde{\sigma}_g)^{0.37}}, \quad (29)$$

plotted as the solid curve in Fig. 3. This expression is obtained by taking the limit $N_2 \rightarrow \infty$ in our formula for $W_g(N_2; \tilde{\sigma}_g)$ (Equation (27)). For large $\tilde{\sigma}_g$, $W_{g,\text{tot}}$ decreases as an increasing fraction of the LW band radiation is absorbed by H₂-dust, before complete line overlap occurs. For $\tilde{\sigma}_g \ll 0.1$, H₂-line absorption dominates, and $W_{g,\text{tot}} \rightarrow W_{d,\text{tot}} \equiv 8.8 \times 10^{13} \text{ Hz}$, independent of $\tilde{\sigma}_g$.

Given our analytic forms for W_g and $W_{g,\text{tot}}$ we can compute the normalized curve of growth $\tilde{w}(N_2) \equiv W_g(N_2)/W_{g,\text{tot}}$. In the lower panel of Fig. 2 we plot \tilde{w} for $\tilde{\sigma}_g = 0.01, 0.1, 1$ and 10. By definition \tilde{w} is normalized such that it approaches unity for large N_2 . Therefore, for any N_2 prior to saturation, \tilde{w} is larger for larger values of $\tilde{\sigma}_g$.

4. DENSITY PROFILES AND TRANSITION POINTS

Starting with Equation (25), we use our analytic procedure, to generate HI and H₂ density profiles for a wide range of αG and σ_g . We are particularly interested in the metallicity behavior so we consider large variations in the dust cross-section. We present results for 4×4 combinations of $\alpha G = 0.01, 0.1, 1$, and 10, and $\tilde{\sigma}_g = 0.01, 0.1, 1$, and 10, where αG and $\tilde{\sigma}_g$ are treated as independent variables. We then use the profiles to derive an analytic scaling relation for the HI-to-H₂ transition points.

4.1. HI and H₂ densities versus gas column

In Fig. 4 we plot (blue solid curves) the atomic and molecular density fractions, n_1/n and $2n_2/n$, as functions of the total gas column density N , for all 4×4 combinations of αG and

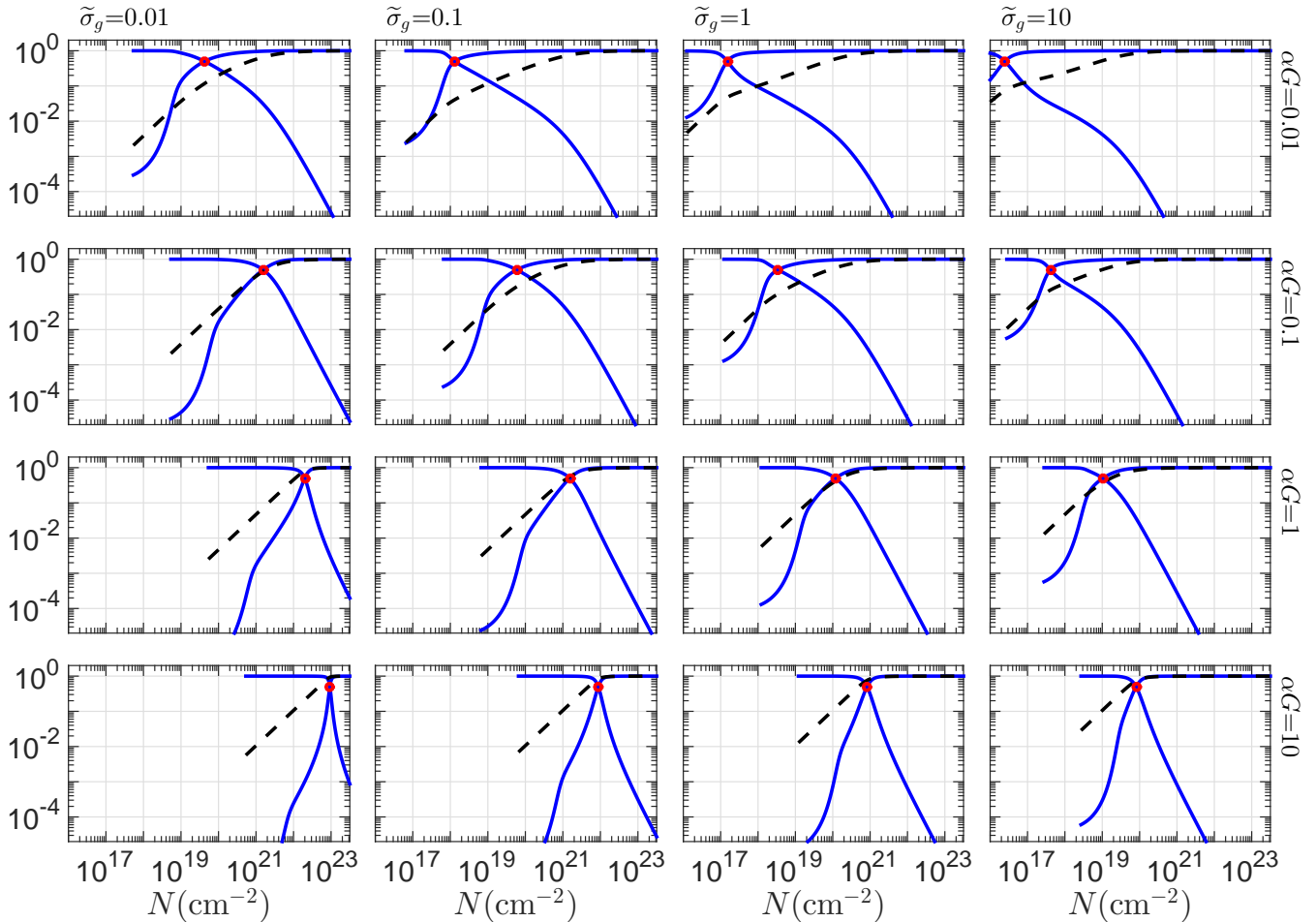


FIG. 4.— The HI and H₂ density profiles n_1/n and $2n_2/n$ (blue solid curves) and the normalized accumulated HI column $\tilde{N}_1(N)$ (dashed black curves), as functions of the total hydrogen column N , for the 4×4 combinations of the basic parameters $\alpha G = 0.01, 0.1, 1, 10$, and $\tilde{\sigma}_g = 0.01, 0.1, 1, 10$. The profiles shown are evaluated through the analytic procedure presented in §3. The HI-to-H₂ transition (red points) occurs at larger depths with increasing αG (stronger UV fields), or decreasing $\tilde{\sigma}_g$ (weaker absorption). The HI-to-H₂ transition is gradual for $\alpha G \ll 1$ and becomes sharp for $\alpha G \gtrsim 1$.

$\tilde{\sigma}_g$. As shown by the curves in each panel, for sufficiently small N the gas is entirely atomic, and for large N the gas is molecular. We define the transition points as the depths at which $n_1 = 2n_2$. These are indicated by the red dots in Fig. 4.

For $N \rightarrow 0$ the ratio $n_1/n_2 \rightarrow \alpha/2 \equiv D_0/(2Rn)$, or equivalently $2n_2/n \rightarrow 4/\alpha$ since $n_1/n \simeq 1$ at the cloud boundaries. We stress that in each row in Fig. 4 it is αG that is held constant, not α . For αG constant, α must be altered with the dust cross-section as $(1 + 8.9\tilde{\sigma}_g)^{0.37}/\tilde{\sigma}_g$. In Fig. 4, this is reflected in the increasing molecular fraction at the cloud boundary, as $\tilde{\sigma}_g$ is increased. For example, for $\alpha G = 0.1$, and for $\tilde{\sigma}_g$ from 0.01 to 10, α decreases from 1.5×10^5 to 7.4×10^3 . The corresponding molecular fractions at the boundaries increase from $2n_2/n = 2.7 \times 10^{-5}$ to 5.3×10^{-3} .

In each panel we also plot (dashed curves) the normalized accumulated HI columns

$$\tilde{N}_1 \equiv \frac{N_1(N)}{N_{1,\text{tot}}}. \quad (30)$$

Here $N_1(N)$ is obtained from step-3 of the procedure (§3), and $N_{1,\text{tot}}$ is the total HI column (Equation (18)). The curves for \tilde{N}_1 show how the HI columns are built up with increasing cloud depth, finally reaching the maximal values when all of the photodissociating radiation has been absorbed. As discussed

by S14, in the strong-field limit ($\alpha G \gtrsim 1$) most of the HI column density is built up in an outer fully photodissociated layer, prior to the conversion points (e.g. see the lowest row in Fig. 4). These are the strong-field “sharp” transitions. In contrast, in the weak-field limit ($\alpha G \lesssim 1$), the transitions are “gradual” and most of the HI column density is built up past the transition points where the gas is predominantly molecular (e.g. see top row in Fig. 4).

In Fig. 4, for any $\tilde{\sigma}_g$, the transition points occur at greater cloud depths as αG is increased, i.e. as the free-space dissociation rate is increased relative to the H₂-formation rate. When αG is small, the transition points are controlled by H₂-self shielding. For large αG , the transition points are limited by HI-dust in addition to self-shielding. For example, for fixed $\tilde{\sigma}_g = 1$, the transition point occurs at gas columns $N_{\text{tran}} = 1.5 \times 10^{17}, 3.5 \times 10^{18}, 1.2 \times 10^{20}$, and $8.3 \times 10^{20} \text{ cm}^{-2}$, for $\alpha G = 0.01, 0.1, 1$, and 10 (top to bottom in Fig. 4).

For fixed αG , the transition points occur at greater gas columns as $\tilde{\sigma}_g$ is reduced. In the strong field limit ($\alpha G \gtrsim 1$), this is simply because the gas column required to achieve a large ($\gtrsim 1$) HI-dust optical depth grows as the dust absorption cross-section is reduced. Thus, for example, for $\alpha G = 10$, the transition column increases from $\sim 10^{20}$ to 10^{23} cm^{-2} , as $\tilde{\sigma}_g$ is reduced from 10 to 0.01 (see bottom row of Fig. 4).

For small αG the behavior is more complicated. Dust ab-

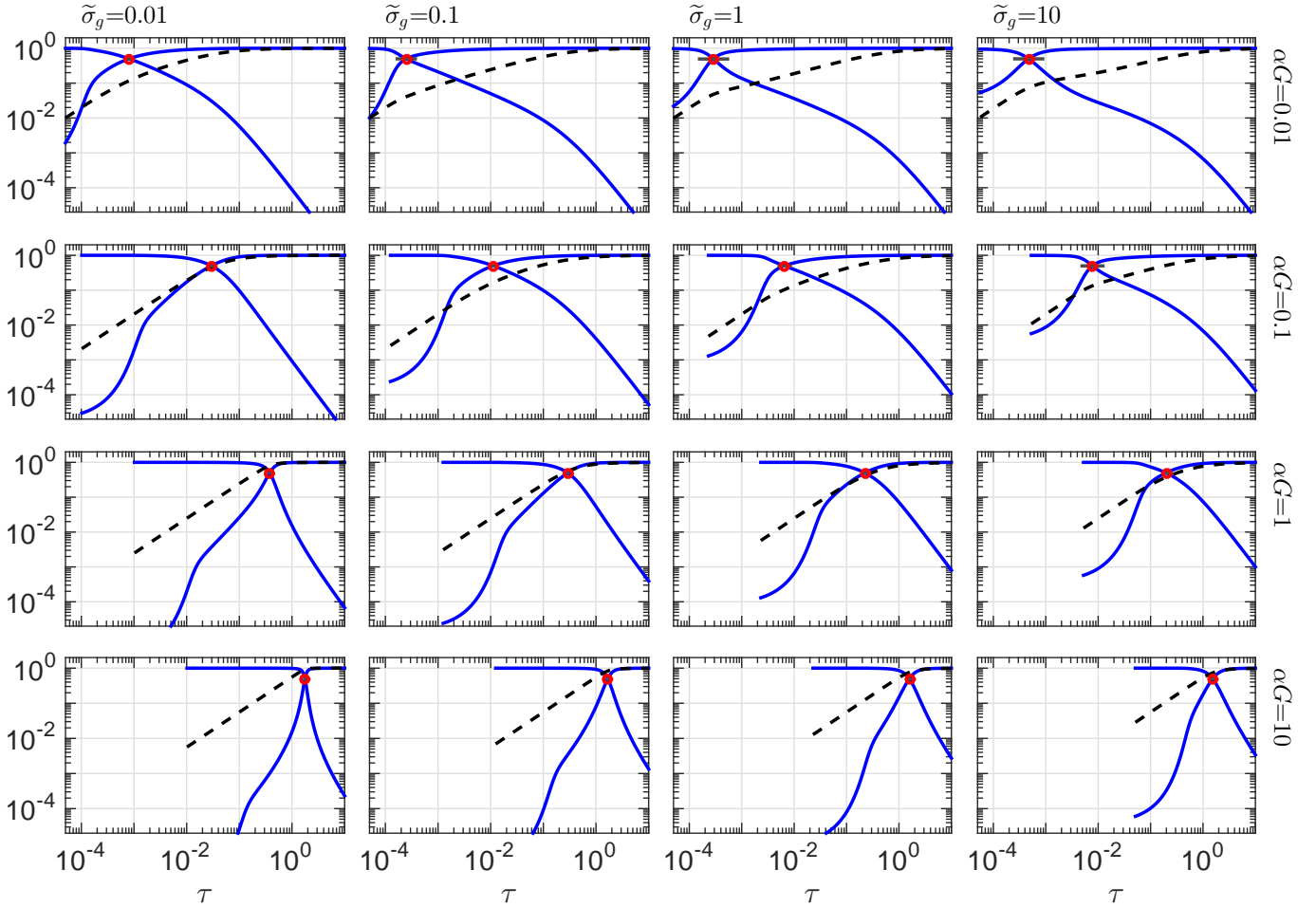


FIG. 5.— The H_I and H₂ density profiles n_1/n and $2n_2/n$ (blue solid curves) and the normalized accumulated H_I column \widetilde{N}_1 (dashed black curves), as functions of the dust opacity $\tau \equiv \sigma_g N$, for the 4×4 combinations of the basic parameters $\alpha G = 0.01, 0.1, 1, 10$, and $\widetilde{\sigma}_g = 0.01, 0.1, 1, 10$. The horizontal bars (mainly seen in the upper right panels) indicate the variation of the transition points for varying Doppler parameter $b_5 = 1$ to 4. The profile shapes (sharp versus gradual) and the positions of the H_I-to-H₂ transition points are determined mainly by the αG parameter.

sorption plays no role, but a dependence on $\widetilde{\sigma}_g$ remains. For example, for $\alpha G = 0.01$, the transitions occur at gas columns equal to 2.5×10^{16} , 1.5×10^{17} , 1.3×10^{18} , and 4.3×10^{19} , as $\widetilde{\sigma}_g$ is reduced from 10 to 0.01 (see top row of Fig. 4). This is because we have assumed that the grain surface H₂ formation rate coefficient, R , is proportional to $\widetilde{\sigma}_g$ (see Equations (9) and (22)), with both quantities scaling in the same way with the dust-to-gas ratio. Thus, for small αG the transition points occur at larger gas columns as $\widetilde{\sigma}_g$ is reduced due to the associated reduction in the H₂ formation efficiency. The behavior is non-linear however, because of the dependence on the H₂ self-shielding function.

Our analytically generated profiles in Fig. 4, and the profiles computed using the full multi-line radiative transfer in S14 (see their Fig. 7) are in excellent agreement.

4.2. HI and H₂ densities versus dust opacity

The overall behavior becomes simpler if the density profiles are plotted as functions of the dust optical depth $\tau \equiv \sigma_g N$, instead of the gas column N . A very useful scaling relation for the transition point is also revealed by making this transformation. In Fig. 5 we show n_1/n , $2n_2/n$ and \widetilde{N}_1 as functions of τ as log-log plots. In Fig. 6 we display the profiles as log-linear plots. The transition points are again indicated by the

red dots.

The dust optical depth at the transition is

$$\tau_{\text{tran}} \equiv \sigma_g (N_{1,\text{tran}} + 2N_{2,\text{tran}}), \quad (31)$$

where $N_{1,\text{tran}}$ and $N_{2,\text{tran}}$ are the integrated atomic and molecular columns up to the transition point (where $n_1 = 2n_2$). As expected, for $\alpha G \gtrsim 1$ H_I-dust absorption becomes significant and $\tau_{\text{tran}} \gtrsim 1$. For $\alpha G \ll 1$, self-shielding dominates and $\tau_{\text{tran}} \ll 1$. Remarkably, as can be seen by inspecting Fig. 5 or 6, for any αG , τ_{tran} is quite insensitive to $\widetilde{\sigma}_g$, especially in the astrophysically important range 0.1 to 10. Indeed to an excellent approximation, the profiles structures depend *only* on αG . This is indicated by the almost identical profiles in each row of Fig. 6 in the linear-log displays that suppress the differences in the free-space H_I/H₂ ratios near the boundaries.

This behavior is not surprising for large αG , for which the transitions all occur at $\tau_{\text{tran}} \sim 1$. However, for small αG this result is less immediate, and depends on the complex interplay between H₂ self-shielding and the connection between the H₂ formation rate coefficient and the dust cross section, and on the definition of the effective dissociation bandwidth.

The precise locations of the transition points do also depend on the assumed absorption-line Doppler parameter when $\alpha G \ll 1$ and $\widetilde{\sigma}_g \gtrsim 1$ since then self-shielding at the transition point occurs near the Doppler cores. In Fig. 5, the horizon-

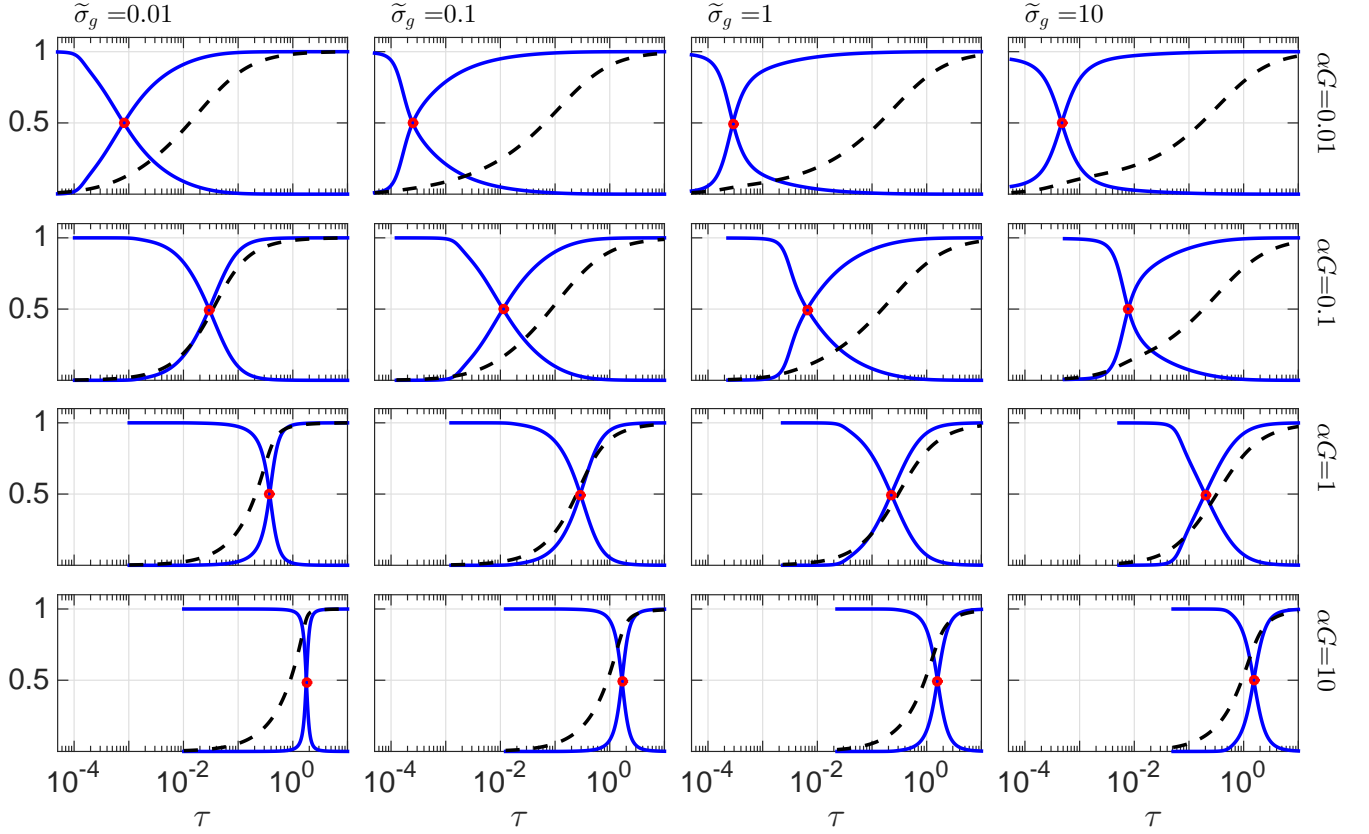


FIG. 6.— H I and H₂ density profiles as functions of dust optical depth in a log-linear display.

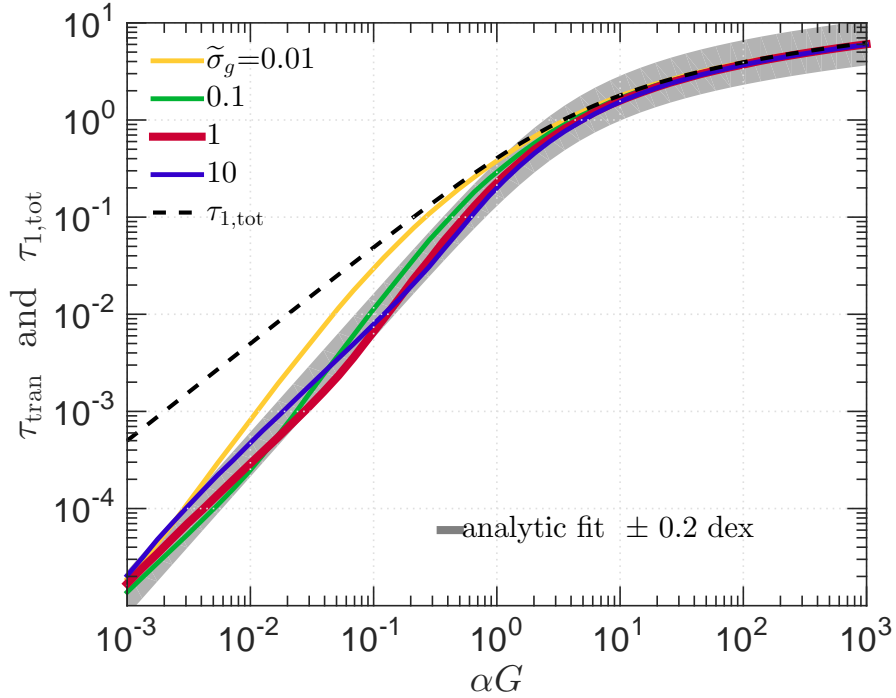


FIG. 7.— The optical depths at the H I-to-H₂ transition points τ_{tran} (the red dots in Fig. 5), as functions of the αG parameter, for $\tilde{\sigma}_g = 0.01, 0.1, 1, 10$ (solid colored curves). For $\tilde{\sigma}_g \gtrsim 0.1$, τ_{tran} depend only weakly on $\tilde{\sigma}_g$ and is determined mainly by the αG parameter. The grey strip is our fitting function given by Equation (39) with $\beta = 0.7$, with a width indicating ± 0.2 dex variations from the formula.

tal bars indicate the variation in the location of the transition points for $b_5 = 1$ to 4 (from left-to-right), a factor of two variation in our assumed Doppler parameter $b_5 = 2$. As $\tilde{\sigma}_g$ becomes small (still at $\alpha G \ll 1$), the self-shielding at the transition points occurs within the damping wings, and the HI-to-H₂ transition is then independent of b .

4.3. Analytic expression for the transition point

That the transition optical depth τ_{tran} depends mainly on the single parameter αG is a primary result of this paper, and we now present an analysis for this behavior.

In Fig. 7 we plot τ_{tran} versus αG ranging from 10^{-3} to 10^3 , for the four values of $\tilde{\sigma}_g$. We computed these curves using our procedure for generating the depth-dependent profiles for any αG , and then extracted the transition points. For comparison, we also plot (dashed curve) the total HI-dust optical depth $\tau_{1,\text{tot}}$ as given by Equation (19) (see also Fig. 1).

For large αG , the curves for τ_{tran} all converge to $\tau_{1,\text{tot}}$ as expected in this limit for which the HI-to-H₂ transitions are sharp. Thus for large αG

$$\tau_{\text{tran}} \simeq \tau_{1,\text{tot}} = \ln \left[\frac{\alpha G}{2} + 1 \right] \simeq \ln \left[\frac{\alpha G}{2} \right] \quad (32)$$

and independent of $\tilde{\sigma}_g$.

For small αG , $\tau_{\text{tran}} \ll \tau_{1,\text{tot}}$, since the transitions are controlled by H₂-self shielding and most of the HI columns are built up past the transition points. Fig. 7 shows that τ_{tran} remains insensitive to $\tilde{\sigma}_g$ even as αG becomes small. For $\tilde{\sigma}_g$ between 0.1 and 10, the transition optical depths do not deviate by more than a factor 2 for any αG down to 10^{-3} . For smaller $\tilde{\sigma}_g$ the transition optical depths increase somewhat as indicated by the curve for $\tilde{\sigma}_g = 0.01$.

This behavior may be understood analytically as follows. When αG is small, $\tau \ll 1$, and dust absorption may be neglected at the transition point. The HI and H₂ column densities at the transition are then given by Equations (11) and (12), evaluated for $n_1 = 2n_2$, giving the pair of equations

$$\frac{n_1}{n_2} = 2 = \frac{1}{2} \alpha f(N_{2,\text{tran}}), \quad (33)$$

and

$$N_{1,\text{tran}} = \frac{\alpha}{2} \frac{W_d(N_{2,\text{tran}})}{\sigma_d}. \quad (34)$$

To obtain simple solutions for the two unknowns $N_{1,\text{tran}}$ and $N_{2,\text{tran}}$, we approximate the H₂ shielding function as a power-law $f \propto N_2^{-\beta}$, so that $W_d \propto N_2^{1-\beta}$ (see Equation (7)). It follows that

$$N_{1,\text{tran}} \propto N_{2,\text{tran}} \propto \alpha^{1/\beta}. \quad (35)$$

The optical depth at the transition point then obeys

$$\tau_{\text{tran}} \propto \tilde{\sigma}_g \alpha^{1/\beta}. \quad (36)$$

If expressed in terms of α alone τ_{tran} is proportional to $\tilde{\sigma}_g$.

To express Equation (36) in terms of αG , we multiply and divide α by $G \propto \tilde{\sigma}_g (1 + 8.9\tilde{\sigma}_g)^{-0.37}$. This gives

$$\tau_{\text{tran}} \propto \tilde{\sigma}_g^{(\beta-1)/\beta} (1 + 8.9\tilde{\sigma}_g)^{0.37/\beta} (\alpha G)^{1/\beta}. \quad (37)$$

Thus, when considering τ_{tran} in terms of αG rather than α , two important limits arise

$$\tau_{\text{tran}} \propto (\alpha G)^{1/\beta} \times \begin{cases} \tilde{\sigma}_g^{(\beta-0.63)/\beta} & \text{for } \tilde{\sigma}_g \gg 0.1 \\ \tilde{\sigma}_g^{(\beta-1)/\beta} & \text{for } \tilde{\sigma}_g \ll 0.1 \end{cases}. \quad (38)$$

As discussed in §3.1, for N_2 in the range $10^{14} - 10^{21} \text{ cm}^{-2}$, $f_{\text{shield}} \propto N_2^{-\beta}$ with $\beta \simeq 0.7$ is a good approximation. The dependence of τ_{tran} on $\tilde{\sigma}_g$ is then very weak, especially for $\tilde{\sigma}_g \gtrsim 0.1$, for which $\tau_{\text{tran}} \propto \tilde{\sigma}_g^{0.10}$. Furthermore, in this approximation τ_{tran} varies as a power-law $(\alpha G)^{1/\beta}$ as seen in Fig. 7.

An excellent fitting formula for τ_{tran} as a function of αG only is therefore

$$\tau_{\text{tran}} = \beta \ln \left[\left(\frac{\alpha G}{2} \right)^{1/\beta} + 1 \right]. \quad (39)$$

For $\alpha G \gg 1$, this gives $\tau_{\text{tran}} \rightarrow \ln[\alpha G/2]$ as it should (Equation (32)). For $\alpha G \ll 1$ the power-law behavior $\tau_{\text{tran}} \propto (\alpha G)^{1/\beta}$ is recovered (Equation (37)), with prefactor β of order unity. The grey strip in Fig. 7 shows τ_{tran} as given by Equation (39) with $\beta = 0.7$, with a width indicating ± 0.2 dex variations from the formula. This choice of β provides best accuracy for $\tilde{\sigma}_g \geq 0.1$. The maximal absolute deviations over the whole αG range are 0.16, 0.21 and 0.20 dex, and the medians (in log space) are 0.03, 0.02 and 0.04 dex, for $\tilde{\sigma}_g = 0.1$, 1, and 10, respectively. For $\tilde{\sigma}_g = 0.01$, the median and maximum absolute deviations are 0.15 dex and 0.49 dex. For factor two variations in the Doppler parameter β varies by less than 5%.

We stress that our universal scaling relation for τ_{tran} depends on the inclusion of the H₂-dust absorption term in the definition of αG , i.e. the $(1 + 8.9\tilde{\sigma}_g)^{-0.37}$ factor. Without this metallicity-dependent term built into the definition of αG , the transition point would depend on αG and σ_g independently.

As examples for how our formula may be used, we compute the gas column density for the transition point for an incident radiation field with $I_{\text{UV}} = 1$, and cloud gas density $n = 10^3 \text{ cm}^{-3}$, assuming a standard gas-to-dust ratio, i.e. $\sigma_g = 1.9 \times 10^{-21} \text{ cm}^2$, and $R = 3 \times 10^{-17} \text{ cm}^3 \text{ s}^{-1}$. For these conditions $\tilde{\sigma}_g = 1$, and $\alpha G = 5.7 \times 10^{-2}$. Plugging into Equation (39) with $\beta = 0.7$ gives $\tau_{\text{tran}} = 4.3 \times 10^{-3}$, or $N_{\text{tran}} = 2.3 \times 10^{18} \text{ cm}^{-2}$. This is only 15% of the total HI column for this value of αG , which is $1.5 \times 10^{19} \text{ cm}^{-2}$. Reducing the metallicity by a factor of 10, and with the assumption that this implies a linear decrease in the dust cross section, this gives $\tilde{\sigma}_g = 0.1$ and $\alpha G = 0.14$, for which $\tau_{\text{tran}} = 1.5 \times 10^{-2}$ and $N_{\text{tran}} = 8.2 \times 10^{19} \text{ cm}^{-2}$.

For $\alpha G = 1$, the critical value between the weak- and strong-field limits, $\tau_{\text{tran}} = 0.22$, and is approximately half the value of $\tau_{1,\text{tot}}$.

4.4. Attenuation factor

Given solutions for the depth dependent atomic and molecular density ratios n_1/n_2 , we can compute the corresponding depth-dependent attenuation factors for the H₂ photodissociation rate. These are given by

$$f_{\text{att}}(N; \alpha G, \tilde{\sigma}_g) = \frac{2}{\alpha} \frac{n_1}{n_2}(N), \quad (40)$$

where as discussed above, any pair $(\alpha G, \tilde{\sigma}_g)$ gives n_1/n_2 versus N , and determines α . In Fig. 8 we plot f_{att} as a function of the total gas column N (left panels) and of the dust opacity $\tau \equiv \sigma_g N$ (right columns). Each panel is for a fixed αG , and shows four curves for the different $\tilde{\sigma}_g$ values. The transition points are marked by the red dots. The crosses indicate the points where the dust opacity $\tau = 1$.

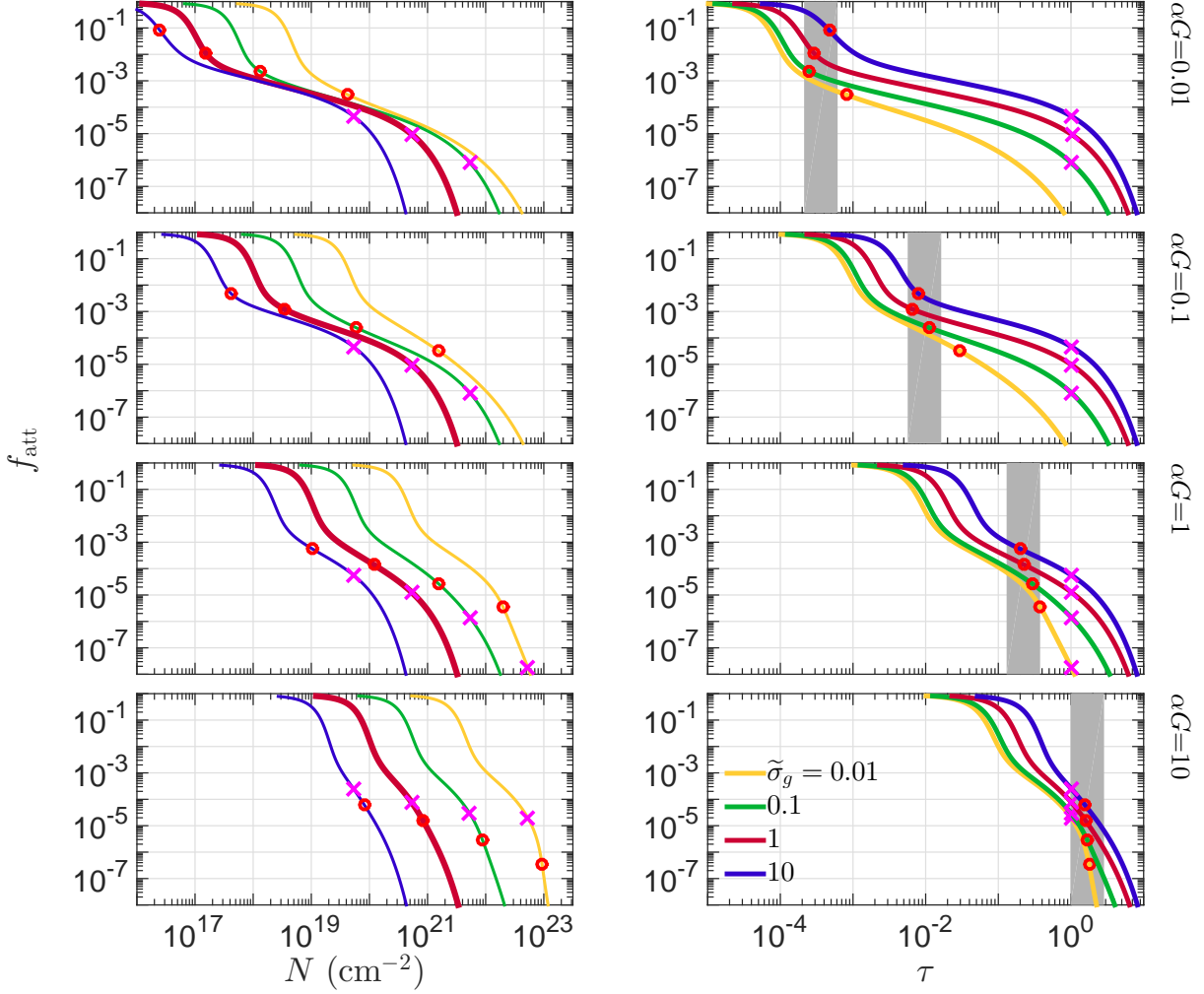


FIG. 8.— The attenuation factor f_{att} as a function of the gas column N (left) and the optical depth τ (right), for $\alpha G = 0.01, 0.1, 1$ and 10 (top to bottom panels), and for $\tilde{\sigma}_g = 0.01, 0.1, 1$ and 10 (color coded). The red circles indicate the HI-to-H₂ transition points. The magenta crosses indicate points of $\tau = 1$.

The curves show the combined effects of H₂-self shielding and dust absorption in reducing the photodissociation rate (recall $f_{\text{att}} \equiv f_{\text{shield}}e^{-\tau}$). For small αG (e.g. upper panel) the curves for $f_{\text{att}}(N)$ resemble $f_{\text{shield}}(N_2)$ (see Fig. 2) for much of the range, because the HI-to-H₂ transition points occur at small gas columns, well before any dust opacity is built up. The sudden onset of self-shielding and drop in the photodissociation rate is followed by a more gradual decline as the H₂ photoabsorption occurs in the line damping wings. Finally, at sufficiently large columns f_{att} drops exponentially due to the H₂-dust cutoff, or due to the complete overlap of the absorption lines. For large αG (e.g. lower panel) the exponential HI-dust cutoff occurs soon after the onset of self-shielding, and the damping wing portions are suppressed. For large αG , most of the LW-band radiation is absorbed by HI-dust. However, self-shielding is still important in reducing the photodissociation rate significantly and enhancing the H₂ fraction within the large atomic layer.

In the right-hand panels of Fig. 8 the vertical grey strips show the predicted positions of the transition points as given by our Equation (36), with a width ± 0.2 dex (as for Fig. 7). For $\tilde{\sigma}_g$ between 0.1 and 10, the computed transition points fall within the strips. For $\tilde{\sigma}_g = 0.01$ the transition points occur at slightly larger dust optical depths, as we have already seen in Fig. 7.

5. HI-TO-H₂ STAR-FORMATION THRESHOLD

We can use our Equation (39) to define a star-formation threshold with the empirically based assumption that conversion to H₂ is required for star-formation, the HI remaining sterile. Following S14 we define the threshold gas mass surface density, $\Sigma_{\text{gas},*}$ ($M_{\odot} \text{ pc}^{-2}$), as the surface density required for half of the mass to be molecular. For our idealized plane-parallel clouds, and for two-sided illumination, the threshold hydrogen gas column $N_{\text{gas},*} \equiv 4N_{\text{tran}} = 4\tilde{\sigma}_g\tau_{\text{tran}}$. Here we are assuming that once the gas becomes predominantly molecular stars can form, even if residual HI exists in the molecular zone as occurs in the weak field limit. Converting to a mass surface density, including the contribution of helium to the mass, gives

$$\Sigma_{\text{gas},*} = \frac{16.5}{\tilde{\sigma}_g} \ln \left[\left(\frac{\alpha G}{2} \right)^{1.43} + 1 \right] M_{\odot} \text{ pc}^{-2}, \quad (41)$$

where we set $\beta = 0.7$ in Equation (39). In Fig. 9 we plot the star-formation thresholds as functions of αG , for $\tilde{\sigma}_g$ from 0.01 to 10. We recall that the dust absorption cross-section may be related to the metallicity, (Equation (5)) with $\sigma_g = 1.9 \times 10^{-21} \phi_g Z' \text{ cm}^2$, or $\tilde{\sigma}_g = \phi_g Z'$, where ϕ_g is a factor of order unity.

For large αG (strong field limit), the HI layers become ex-

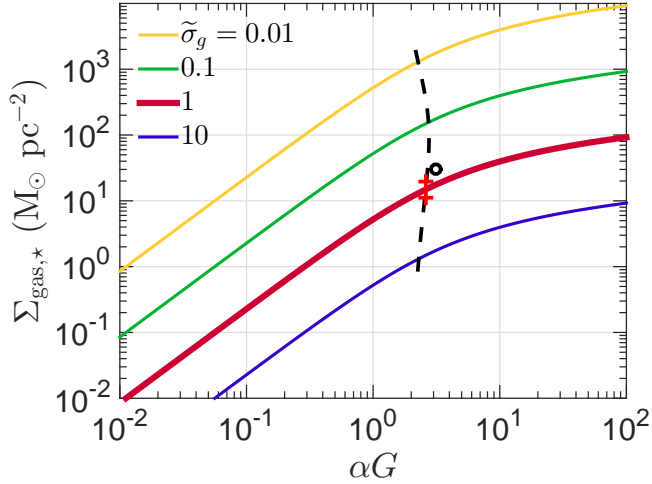


FIG. 9.— Star-formation thresholds as functions of αG , for $\tilde{\sigma}_g = 0.01, 0.1, 1, \text{ and } 10$. The dashed curve is the locus $\alpha G = (\alpha G)_{\text{CNM}}$ (see text). The red crosses are the thresholds predicted by S14 for beamed (upper) and isotropic (lower) irradiation. The black circle is the threshold derived by McKee & Krumholz (2010).

tended but are limited by HI-dust absorption. For example for $\tilde{\sigma}_g = 1$ (or $Z' \approx 1$), $\Sigma_{\text{gas},*}$ increases from 5 to 92 $M_\odot \text{ pc}^{-2}$ for αG from 1 to 10^2 . For low αG (weak field limit) the outer HI layers become very narrow and $\Sigma_{\text{gas},*}$ drops sharply. For $\tilde{\sigma}_g = 1$, $\Sigma_{\text{gas},*}$ decreases from 5 to $8 \times 10^{-2} M_\odot \text{ pc}^{-2}$ for $\alpha G = 1$ to 10^{-2} . Because the dust optical depth at the HI-to- H_2 conversion point is insensitive to $\tilde{\sigma}_g$, the threshold surface-density varies with metallicity as $1/Z'$ for any αG .

If the HI gas is assumed to be cold (CNM) at multiphased conditions (Krumholz, McKee & Tumlinson 2008; S14) then $\alpha G = (\alpha G)_{\text{CNM}}$ in Equation (41), where as given by S14⁴

$$(\alpha G)_{\text{CNM}} \equiv 2.6 \left(\frac{1 + 3.1Z'^{0.365}}{4.1} \right) \left(\frac{9.9}{1 + 8.9\phi_g Z'} \right)^{0.37}. \quad (42)$$

The dashed curve in Fig. 9 shows the locus $\alpha G = (\alpha G)_{\text{CNM}}$ for Z' from 10 to 0.01 (assuming $\phi_g = 1$). For $\tilde{\sigma}_g = 1$ ($Z' \approx 1$), and for $\alpha G = (\alpha G)_{\text{CNM}}$, the threshold surface density is 15 $M_\odot \text{ pc}^{-2}$.

S14 gave expressions for the thresholds $\Sigma_{\text{gas},*}$ but with τ_{tran} replaced by $\tau_{1,\text{tot}}$, with the added assumption (valid for $\alpha G \gtrsim 1$) that the transitions are sharp. The upper and lower red crosses in Fig. 9 are the predicted S14 thresholds, equal to 11 and 20 $M_\odot \text{ pc}^{-2}$, for $\alpha G = (\alpha G)_{\text{CNM}}$ and $\tilde{\sigma}_g = 1$, for beamed and isotropic irradiation respectively. The circle shows the McKee & Krumholz (2010) result of 30 $M_\odot \text{ pc}^{-2}$, for their assumed $(\alpha G)_{\text{CNM}} = 3.1$ for solar metallicity, and assuming spherical geometry⁵.

In general, the assumption that $\alpha G = (\alpha G)_{\text{CNM}}$ may be too restrictive, e.g. as shown for the HI-to- H_2 transitions in the Perseus molecular cloud (Bialy et al. 2015). Our Equation (41) provides estimates for the thresholds for arbitrary αG and metallicity.

⁴In this expression we have adjusted Eq. (59) of S14 for $(\alpha G)_{\text{CNM}}$ by using our adopted formula Eq. (29) for $W_{g,\text{tot}}$, instead of Eq. (28)

⁵S14 present (§4) a detailed comparison between the formulae and results for slab geometry versus the spheres assumed by Krumholz, McKee & Tumlinson (2009); McKee & Krumholz (2010).

In this paper we have extended the analytic theory presented by Sternberg et al. (2014, S14) for the HI-to- H_2 transitions in interstellar photon dominated regions (PDRs), to develop a simple procedure for the construction of steady-state HI-to- H_2 density profiles for FUV irradiated clouds. Following S14, we first demonstrate that for uniform density gas, and for a steady irradiation fluxes, the atomic to molecular gas fractions as functions of cloud depth, in one-dimensional slabs, depend on two basic parameters. First is the dimensionless “ αG parameter” (Sternberg 1988; S14) that determines the dust optical depth associated with the total photodissociated HI column. Second is $\tilde{\sigma}_g$, the dust-grain absorption cross-section per hydrogen nucleus in the 1100 to 912 Å Lyman-Werner photodissociation band. The αG parameter is proportional to the ratio of the FUV field intensity to the gas density, or alternatively to the ratio of the H_2 dissociation rate to the molecular formation rate (see Equations (20) and (21)). The dust-grain absorption cross-section also enters into the definition of αG because some of the LW band radiation may be absorbed by dust associated with just the H_2 .

We then develop our analytic procedure for generating HI-to- H_2 density profiles. It may be used for arbitrary input gas density, FUV field intensity, H_2 formation rate coefficient and dust-grain absorption cross-section. The gas density and field intensity may vary widely in differing interstellar environments. The formation rate coefficient and dust absorption cross-section will generally vary with the metallicity dependent dust-to-gas ratio. Our simple 5-step procedure (§3) requires analytic forms for (a) the H_2 -self shielding function, (b) the dust limited curve-of-growth for multiline dissociation bandwidth, and (c) the total dust-limited bandwidths. We develop the required analytic expressions for (b) and (c) (Equations (27) and (29)) based on the detailed radiative transfer results presented by S14. For (a) we recommend the Draine & Bertoldi (1996) formula (Equation (26)).

We use our procedure to generate a 4×4 set (Fig. 4) of HI-to- H_2 transition profiles, showing the fractions as functions of the total gas columns, from large (strong-field) to small (weak-field) αG , and for dust cross-sections ranging from super-solar to very low dust-to-gas mass ratios. We then show that if the profiles are displayed (Figs. 5-6) as functions of the dust optical depth (or visual extinction) the dependence on $\tilde{\sigma}_g$ becomes very weak, and just αG remains as the single controlling parameter, including also for the depth at which the HI-to- H_2 transition occurs. This simple scaling behavior is valid from the strong-field limit where HI-dust opacity dominates at the transition point, to the weak-field limit where the transition is controlled by self-shielding only.

We use our results to derive a simple universal fitting formula for the dust optical depth at which the HI-to- H_2 transition occurs, as a function of the single dimensionless parameter αG (Equation (39) and Fig. 7). We use our formula for the transition depth to develop an expression for the threshold gas mass surface density required for star-formation, under the assumption that individual clouds become star-forming when $\sim 50\%$ of the gas mass is molecular (Equation (41) and Fig. 9).

Our analytic procedure and formulae for the HI-to- H_2 transition points and star-formation thresholds will be useful for interpreting observations of interstellar HI/ H_2 interfaces on small and global galactic scales, and for incorporation into hydrodynamics simulations.

We thank Frank Le Petit and Evelyne Roueff for in-depth discussions about this work, and the referee for helpful comments that improved our presentation. We thank Chris McKee for comments, and Henrik Beuther and Thomas Henning for stimulating conversations. We thank Or Shrim for his assis-

tance in generating the HI and H₂ density profiles. S.B. acknowledges support from the Raymond and Beverly Sackler Tel Aviv University – Harvard/ITC Astronomy Program. This work was supported by the PBC Israel Science Foundation I-CORE Program grant 1829/12.

REFERENCES

- Allen R. J., Heaton H. I., Kaufman M. J., 2004, *ApJ*, 608, 314
 Allers K. N., Jaffe D. T., Lacy J. H., Draine B. T., Richter M. J., 2005, *ApJ*, 630, 368
 Bahe Y. M. et al., 2015, *ArXiv e-prints*
 Barriault L., Joncas G., Lockman F. J., Martin P. G., 2010, *MNRAS*, 407, 2645
 Bialy S., Sternberg A., 2015, *MNRAS*, 450, 4424
 Bialy S., Sternberg A., Lee M.-Y., Le Petit F., Roueff E., 2015, *ApJ*, 809, 122
 Bialy S., Sternberg A., Loeb A., 2015, *ApJ*, 804, L29
 Bigiel F., Leroy A., Walter F., Brinks E., de Blok W. J. G., Madore B., Thornley M. D., 2008, *AJ*, 136, 2846
 Bühr S. et al., 2015, *AA*, 580, A112
 Bisbas T. G., Bell T. A., Viti S., Yates J., Barlow M. J., 2012, *MNRAS*, 427, 2100
 Blitz L., Rosolowsky E., 2004, *ApJ*, 612, L29
 Browning M. K., Tumlinson J., Shull J. M., 2003, *ApJ*, 582, 810
 Cazaux S., Spaans M., 2004, *ApJ*, 611, 40
 Davé R., Katz N., Oppenheimer B. D., Kollmeier J. A., Weinberg D. H., 2013, *MNRAS*, 434, 2645
 Draine B. T., 1978, *ApJS*, 36, 595
 Draine B. T., 2003, *ApJ*, 598, 1017
 Draine B. T., Bertoldi F., 1996, *ApJ*, 468, 269
 Federman S. R., Glassgold A. E., Kwan J., 1979, *ApJ*, 227, 466
 Glover S. C. O., Clark P. C., 2012, *MNRAS*, 421, 9
 Glover S. C. O., Federrath C., Mac Low M.-M., Klessen R. S., 2010, *MNRAS*, 404, 2
 Gnedin N. Y., Draine B. T., 2014, *ApJ*, 795, 37
 Gnedin N. Y., Tassis K., Kravtsov A. V., 2009, *ApJ*, 697, 55
 Goicoechea J. R., Le Bourlot J., 2007, *A&A*, 467, 1
 Herbst E., Klemperer W., 1973, *ApJ*, 185, 505
 Hollenbach D., McKee C. F., 1979, *ApJS*, 41, 555
 Kaufman M. J., Wolfire M. G., Hollenbach D. J., Luhman M. L., 1999, *ApJ*, 527, 795
 Krumholz M. R., Leroy A. K., McKee C. F., 2011, *ApJ*, 731, 25
 Krumholz M. R., McKee C. F., Tumlinson J., 2008, *ApJ*, 689, 865
 Krumholz M. R., McKee C. F., Tumlinson J., 2009, *ApJ*, 693, 216
 Lagos C. d. P. et al., 2015, *MNRAS*, 452, 3815
 Le Bourlot J., Le Petit F., Pinto C., Roueff E., Roy F., 2012, *A&A*, 541, A76
 Lee M.-Y., Stanimirović S., Murray C. E., Heiles C., Miller J., 2015, *ApJ*, 809, 56
 Leroy A. K., Walter F., Brinks E., Bigiel F., de Blok W. J. G., Madore B., Thornley M. D., 2008, *AJ*, 136, 2782
 Liszt H. S., 2007, *A&A*, 461, 205
 Liszt H. S., 2015, *ApJ*, 799, 66
 Mac Low M.-M., Glover S. C. O., 2012, *ApJ*, 746, 135
 Maloney P. R., Hollenbach D. J., Tielens A. G. G. M., 1996, *ApJ*, 466, 561
 McKee C. F., Krumholz M. R., 2010, *ApJ*, 709, 308
 Meijerink R., Spaans M., 2005, *A&A*, 436, 397
 Rémy-Ruyer A. et al., 2014, *A&A*, 563A, 31
 Robertson B. E., Kravtsov A. V., 2008, *ApJ*, 680, 1083
 Rodríguez-Fernández N. J., Martín-Pintado J., Fuente A., de Vicente P., Wilson T. L., Hüttemeister S., 2001, *A&A*, 365, 174
 Rosenthal D., Bertoldi F., Drapatz S., 2000, *A&A*, 356, 705
 Schrub A. et al., 2011, *AJ*, 142, 37
 Shaw G., Ferland G. J., Henney W. J., Stancil P. C., Abel N. P., Pellegrini E. W., Baldwin J. A., van Hoof P. A. M., 2009, *ApJ*, 701, 677
 Sheffer Y., Wolfire M. G., Hollenbach D. J., Kaufman M. J., Cordier M., 2011, *ApJ*, 741, 45
 Sternberg A., 1988, *ApJ*, 332, 400
 Sternberg A., Dalgarno A., 1995, *ApJS*, 99, 565
 Sternberg A., Le Petit F., Roueff E., Le Bourlot J., 2014, *ApJS*, 790, 10S
 Thompson R., Nagamine K., Jaacks J., Choi J.-H., 2014, *ApJ*, 780, 145
 Tielens A. G. G. M., 2013, *Reviews of Modern Physics*, 85, 1021
 Timmermann R., Bertoldi F., Wright C. M., Drapatz S., Draine B. T., Haser L., Sternberg A., 1996, *A&A*, 315, L281
 Valdivia V., Hennebelle P., 2014, *A&A*, 571, A46
 van Dishoeck E. F., Black J. H., 1986, *ApJS*, 62, 109
 van Dishoeck E. F., Herbst E., Neufeld D. A., 2013, *Chemical reviews*, 113, 9043
 Wong T., Blitz L., 2002, *ApJ*, 569, 157